

Temporally resolved aortic 3D shape reconstruction from a limited number of cine 2D MRI slices

Gloria Wolkerstorfer¹, Stefano Buoso¹, Rabea Schlenker^{1,2}, Jochen von Spiczak^{1,3}, Robert Manka^{1,2,3}, Sebastian Kozerke¹

¹*Institute for Biomedical Engineering, University Zurich and ETH Zurich, Zurich, Switzerland*

²*Department of Cardiology, University Heart Center, University Hospital Zurich, University of Zurich, Zurich, Switzerland*

³*Diagnostic and Interventional Radiology, University Hospital Zurich, University of Zurich, Zurich, Switzerland*

Abstract

Background and Objective: We propose a shape reconstruction framework to generate time-resolved, three-dimensional patient-specific aortic geometries from a limited number of standard cine 2D magnetic resonance imaging (MRI) acquisitions. To this end, a statistical shape model of the aorta is coupled to a differentiable volumetric mesh optimization algorithm to obtain personalized aortic meshes.

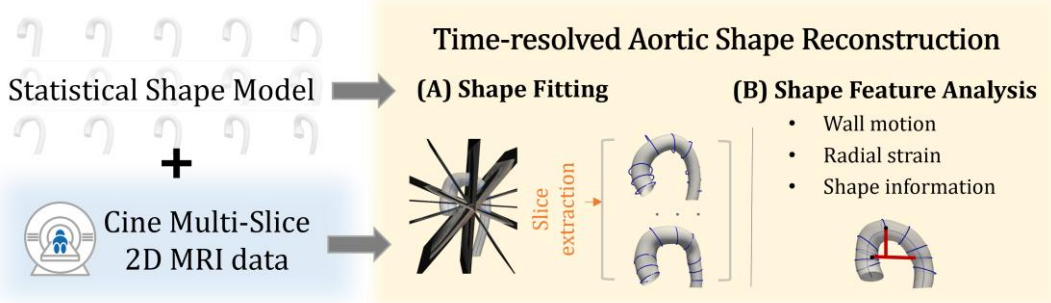
Methods: Initially, the statistical shape model was constructed and 2D slice placements along the aortic arch were studied using a retrospective dataset and, based on the optimized positions, cine 2D MRI slices were acquired in a cohort of 30 subjects (19 volunteers and 11 aortic stenosis patients). Upon manual segmentation of the 2D MRI slices, time-resolved aortic models were derived using differentiable volumetric mesh optimization to obtain vessel shape information, centerline parameters and radial wall strains. In a subset of 10 subjects, additional 4D flow MRI data was acquired to compare peak-systolic aortic shapes against the shapes derived from 2D MRI slices using the proposed method.

Results: Results show that anatomically accurate aortic shapes can be derived from as few as six cine 2D MRI slices using the proposed shape reconstruction method, achieving a mean \pm standard deviation Dice score of (89.9 ± 1.6) %, Intersection over Union of (81.7 ± 2.7) %, Hausdorff distance of (7.3 ± 3.3) mm, and Chamfer distance of (3.7 ± 0.6) mm relative to 4D flow MRI references. The mean absolute radius error along the arch relative to 4D flow MRI was (0.8 ± 0.6) mm. Significant differences between age groups (young, mid-age, elderly) were observed for all shape features, including radial strain. Radial strain decreased progressively with age, with values of $(11.00 \pm 3.11) \times 10^{-2}$ vs. $(3.74 \pm 1.25) \times 10^{-2}$ vs. $(2.89 \pm 0.87) \times 10^{-2}$ for the young, mid-age, and elderly groups, respectively.

Conclusion: It is concluded that the present approach allows for efficient extraction of time-resolved aortic 3D meshes, suitable for various computational downstream tasks, from limited sets of standard cine 2D MRI acquisitions.

Highlights:

- Generation of time-resolved 3D aortic computational meshes from a limited set of standard cine 2D MRI slices using differentiable statistical shape modelling and mesh optimization.
- Aortic shapes derived from as few as six standard cine 2D MRI slices compare well with shapes extracted from non-standard 4D flow MRI data.
- Quantitative metrics are readily derived including vessel shape parameters and radial wall strain.



1 Introduction

Patient-specific computational models of cardiovascular anatomy are increasingly used for geometric analysis, biomechanical simulation, and individualized research applications [1–3]. In the context of the aorta, accurate reconstruction of time-resolved three-dimensional geometries is essential for studying morphological variation [4–7], wall motion [8–10], disease-associated remodelling [11], and used for personalized in-silico biophysical simulations [12]. Therefore, it is critical to develop efficient approaches to derive time-resolved 3D aortic shapes [13, 14].

Statistical shape models (SSMs) provide a framework to capture anatomical variability by representing anatomical structures through a set of principal modes, describing statistically meaningful shape variation. SSMs of the aorta have been developed in several studies, primarily using static volumetric Computed Tomography (CT) and MRI data as input, to characterize specific pathologies and quantify morphological differences [15, 16]. Despite these advances, efficient patient-specific time-resolved 3D shape reconstruction from standard cine 2D MRI imaging has, to the best of our knowledge, not yet been applied to the aorta – while its utility in cardiac modelling has been established [17, 18].

Cardiovascular magnetic resonance imaging using 2D multi-slice balanced steady-state free precession (bSSFP) and spoiled gradient-echo (GRE) sequences is a standard clinical modality for anatomical and functional assessment of the heart and surrounding vessels, such as the aorta [19]. The aortic shape is typically imaged using a 3D bSSFP or GRE scan, however, without capturing its temporal variation during the cardiac cycle. In the research setting, 4D flow MRI enables volumetric, time-resolved blood flow and shape quantification [20, 21]. However, its limited spatial (~ 2.5 mm) 3 and temporal (40–50 ms) resolution, prolonged acquisition and reconstruction times, and low vessel-to-background contrast can hinder vessel wall segmentation and motion analysis [22, 23]. Accordingly, existing segmentation approaches often rely on peak-systolic cardiac frames [24, 25], with Dice scores typically ranging between 0.83 and 0.92 on non-contrast enhanced data [26–29]. Additionally, the availability of 4D flow MRI sequences and efficient post-processing pipelines is often limited in the clinical setting. Instead of using 4D flow MRI, a recent study investigated time-resolved 3D bSSFP sequences for anatomical aortic shape extraction [30]. While the approach shows promise, it is not yet available in clinical routine, also due to its extended data acquisition and reconstruction times.

The present work proposes a method for generating subject-specific, time-resolved aortic meshes by fitting a statistical shape model to a limited set of cine 2D MRI slices. Unlike volumetric or 4D acquisitions, which require extended scan time and specialized post-processing, cine 2D imaging is widely implemented in clinical cardiac MRI and provides high spatial and temporal resolution. By leveraging these routinely acquired views, the proposed framework enables reconstruction of dynamic aortic geometries without additional imaging burden. The present study focuses on methodological feasibility and validation against volumetric reference data.

2 Materials and Methods

In this work, time-resolved cross-sectional segmentations serve as input to a differentiable volumetric mesh optimization process for generating subject-specific geometric representations suitable for downstream shape and strain analysis (Figure 1).

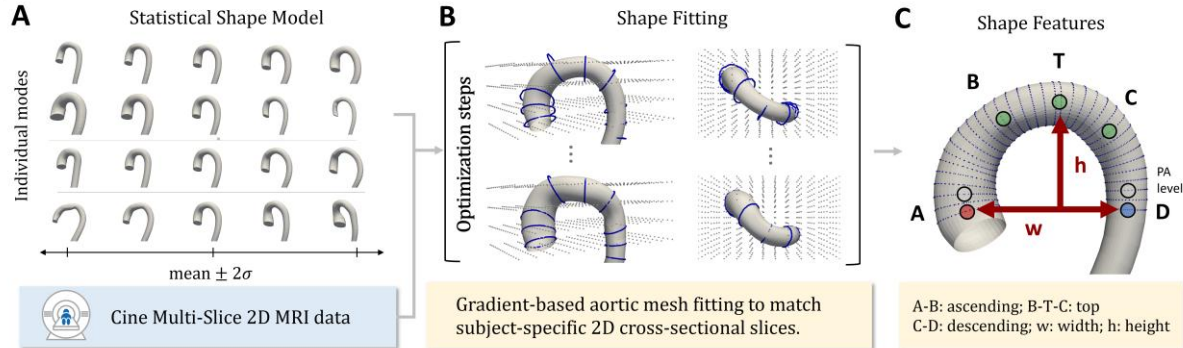


Figure 1: Overview of temporally resolved aortic 3D shape reconstruction: (A) a statistical shape model and segmentations of standard cine multi-slice 2D MRI data acquired along the aorta serve as input to (B) a differentiable volumetric mesh optimization algorithm yielding (C) computational meshes for various downstream tasks of shape analysis.

2.1 Statistical shape model

The statistical shape model was derived using a publicly available dataset comprising of 3000 synthetic aortic shapes, generated from 26 CT-based aortic meshes, obtained from patients diagnosed with aortic valve stenosis, with an age range of 78 to 89 years [16]. The dataset was chosen due to its high-quality mesh connectivity and anatomical coverage. To streamline processing and to exclude the aortic root, each mesh was clipped at the sinotubular junction and remeshed to a standardized grid with $N = 3280$ nodes and 6478 cells comprised in 40 cross-sections with 82 points each, ensuring a consistent topology. The SSM was generated using principal component analysis (PCA), capturing the primary modes of anatomical variation across the dataset. Weighted linear combinations of these PCA modes enabled geometric reconstruction. Figure 1A illustrates the SSM's expressivity by demonstrating the effect of varying the weights of the four dominant modes. For the subsequent differentiable volumetric mesh optimization (Figure 1B), the first ten modes ($M = 10$), accounting for 98.5 % of the total variation, were included.

2.2 Shape fitting

To generate subject-specific aortic geometries, we adapted a method originally developed by Joyce et al [17] for left ventricular modelling. This approach couples a SSM with a differentiable volumetric mesh fitting algorithm, that optimizes mesh vertices to align with subject-specific 2D cross-sectional segmentations (Figure 1B). The algorithm is outlined in Figure 2. In brief, the SSM mean shape, $X_{mean} \in \mathbb{R}^{N \times 3}$, is first centered within a 3D Cartesian coordinate system. A total of S segmented contours are extracted from the 2D image slices. Each contour is uniformly interpolated to $P = 180$ points, resulting in a combined set of slices $s \in \mathbb{R}^{Q \times 3}$, where $Q = S \times P$. These points are then positioned in the same 3D space (visualized as blue contours in Figure 1B). A regular grid of control points $c \in \mathbb{R}^{K \times 3}$, with $K = 720$, is initialized around the mesh (shown as gray points in Figure 1B). For each iteration i , the predicted mesh is updated by combining (i) global shape variations captured by the SSM and rigid transformations, as well as (ii) local deformations propagated from the surrounding control points. Specifically, for every time frame t we first compute the mesh coordinates predicted by the SSM as:

$$\mathbf{X}_{PCA}(t) = \mathbf{X}_{mean} + \delta(t) \sum_{m=1}^M a_m(t) \sigma_{PCA_m} \Phi_m,$$

where $\delta \in \mathbb{R}$ is a scalar, controlling deformation of the magnitude, and $\mathbf{a} \in \mathbb{R}^M$, $\sigma_{PCA} \in \mathbb{R}^M$, $\Phi \in \mathbb{R}^{M \times N \times 3}$ are the amplitudes, standard deviations and basis vectors of the PCA model. The coordinates given by the SSM are then translated, rotated and scaled as:

$$\mathbf{X}_{TRANS}(t) = \psi(t) \mathbf{X}_{PCA}(t) \cdot \mathbf{R}(\alpha(t), \beta(t), \gamma(t)) + \mathbf{o}(t),$$

where $\psi(t) \in \mathbb{R}$ determines an isotropic scaling, $\mathbf{R} \in \mathbb{R}^{3 \times 3}$ is the rotation matrix function of the Euler angles $(\alpha(t), \beta(t), \gamma(t))$, and $\mathbf{o}(t) \in \mathbb{R}^{N \times 3}$ is a translation offset. Local deformations of point coordinates $\mathbf{x}(x, y, z) \in \mathbf{X}_{TRANS}$, are refined using radial basis function (RBF) interpolation with polyharmonic splines. The deformation field $RBF(\mathbf{x}, \mathbf{c}, \Delta\mathbf{c})$ can be modelled as:

$$RBF(\mathbf{x}, \mathbf{c}, \Delta\mathbf{c}) = \sum_{k=1}^K \omega_k \|\mathbf{x} - (\mathbf{c}_k + \Delta\mathbf{c}_k)\| + \mathbf{v}^T \tilde{\mathbf{x}}, \quad \text{where } \tilde{\mathbf{x}} = \begin{bmatrix} \mathbf{x} \\ 1 \end{bmatrix},$$

where \mathbf{c} are the fixed control points, $\Delta\mathbf{c}$ their learned offsets, $\omega \in \mathbb{R}^{K \times 3}$ are the RBF weights, and $\mathbf{v} \in \mathbb{R}^{4 \times 3}$ is the linear coefficient matrix including bias. It should be noted that the weight and bias matrices are reinitialized and updated independently at every iteration.

Finally, the mesh update $\mathbf{X}(t)$ is then computed as:

$$\mathbf{X}(t) = \mathbf{X}_{TRANS}(t) + RBF(\mathbf{X}_{TRANS}(t), \mathbf{c}, \Delta\mathbf{c}(t)).$$

Here, the only fixed parameters in the model are \mathbf{X}_{mean} , Φ , σ_{PCA} and the initial control point positions \mathbf{c} . All other parameters are optimized throughout the process. The optimization is driven by the following loss function:

$$\mathcal{L}_{tot}(t) = \mathcal{L}_{mesh}(t) + \mathcal{L}_{centerline}(t) + \mathcal{L}_{modal}(t) + \mathcal{L}_{rot}(t) + \mathcal{L}_{warp}(t).$$

The mesh loss is defined by minimizing the squared L_2 norm distance between each of the mesh surface points $\mathbf{x}(t)$ and closest 2D slice contours $\mathbf{s}(t)$:

$$\mathcal{L}_{mesh}(t) = \frac{1}{Q} \sum_{j=1}^Q \min_{\mathbf{x} \in \mathbf{X}(t)} \|\mathbf{s}(t)_j - \mathbf{x}(t)\|^2.$$

The centerline loss, $\mathcal{L}_{centerline}$, enforces alignment between the mesh-derived centerline, $\mathbf{cl}_{mesh}(t) \in \mathbb{R}^{P_m \times 3}$, interpolated to $P_m = 500$ points, and the data-derived centerline, $\mathbf{cl}_{slices}(t) \in \mathbb{R}^{P_s \times 3}$, which is obtained by fitting a B-spline through the centers of mass of the segmented contours to $P_s = 300$ points (using SciPy [31]). It is defined as:

$$\mathcal{L}_{centerline}(t) = \frac{1}{P_s} \sum_{i=1}^{P_s} \min_{j \in P_m} \|\mathbf{cl}_{slices}(t)_i - \mathbf{cl}_{mesh}(t)_j\|^2,$$

implicitly optimizing parameters of scaling and translation. \mathcal{L}_{modal} , \mathcal{L}_{rot} and \mathcal{L}_{warp} are regularization losses minimizing the mean-squared modal amplitudes $\mathbf{a}(t)$, rotation angles $(\alpha(t), \beta(t), \gamma(t))$ and control point displacements $\Delta\mathbf{c}(t)$ as:

$$\mathcal{L}_{modal}(t) = \frac{1}{M} \sum_{m=1}^M a_m(t)^2,$$

$$\mathcal{L}_{rot}(t) = \frac{1}{3} \sum \mathbf{R}(\alpha(t), \beta(t), \gamma(t))^2,$$

$$\mathcal{L}_{warp}(t) = \frac{1}{K} \sum_{k=1}^K \Delta \mathbf{c}_k(t)^2.$$

Due to the hierarchical significance of the different loss terms, we used selective activation of learnable parameters across a total of 300 epochs. Given spatiotemporal correlation over the cardiac cycle, shapes of subsequent cardiac frames were fitted using the last 50 epochs of the algorithm, initialized with each previously fitted one. The algorithm was implemented using PyTorch [32] and the Adam optimizer [33] with a learning rate of 0.1 was deployed.

Algorithm 1: Shape fitting pseudo code

Input: $\mathbf{X}_{\text{mean}}, \Phi, \mathbf{a}^{\text{init}}, \sigma_{\text{PCA}}, \delta^{\text{init}}, \mathbf{s}(t)$
Output: Personalized mesh $\mathbf{X}(t)$ and centerline $\mathbf{cl}_{\text{mesh}}(t)$

for frame t in cardiac cycle **do**

- Load cross-sectional slices $\mathbf{s}(t)$ and compute centerline $\mathbf{cl}_{\text{slices}}(t)$
- Center data by subtracting center of mass
- if** $t = 0$ **then**
 - Initialize **meshFitter** with SSM data and centered \mathbf{c} :
 - $[\mathbf{a}(t_0^i), \delta(t_0^i)] \leftarrow [\mathbf{a}(t_0^{\text{init}}), \delta(t_0^{\text{init}})]$
 - for** epoch i to 300 **do**
 - if** $i < 10$: learn $\leftarrow [\mathbf{a}(t_0^i), \delta(t_0^i)]$
 - elif** $10 < i < 200$: learn $\leftarrow [\mathbf{a}(t_0^i), \delta(t_0^i), \psi(t_0^i), \mathbf{R}(t_0^i), \mathbf{o}(t_0^i)]$
 - elif** $200 < i < 250$: learn $\leftarrow [\mathbf{a}(t_0^i), \delta(t_0^i), \mathbf{R}(t_0^i), \Delta \mathbf{c}(t_0^i)]$
 - else**: learn $\leftarrow [\Delta \mathbf{c}(t_0^i)]$
 - $\mathbf{X}_{\text{PCA}}(t_0^i) = \mathbf{X}_{\text{mean}} + \delta(t_0^i) \sum_{m=1}^M a_m(t_0^i) \sigma_{\text{PCA}_m} \Phi_{m,n}$
 - $\mathbf{X}_{\text{TRANS}}(t_0^i) = \psi(t_0^i) \cdot \mathbf{X}_{\text{PCA}}(t_0^i) \cdot \mathbf{R}(t_0^i) + \mathbf{o}(t_0^i)$
 - $\mathbf{X}(t_0^i) = \text{RBF}(\mathbf{X}_{\text{TRANS}}(t_0^i), \mathbf{c}, \Delta \mathbf{c}_i^0)$
- else**
 - Fine-tune based on previous frame:
 - for** epoch i to 50 **do**
 - learn $\leftarrow [\Delta \mathbf{c}(t_t^i)]$
 - $\mathbf{X}(t_t^i) = \text{RBF}(\mathbf{X}(t_{-1}^i), \mathbf{c}, \Delta \mathbf{c}(t_{-1}^i))$

Predict: mesh points \leftarrow model()
Compute \mathcal{L}_{tot} and update model

Figure 2: Pseudo code for the shape fitting process.

The SSM mesh processing and shape fitting code is available in the accompanying online repository.

2.3 In-vivo MRI data acquisition

Prospective MRI data was acquired in a total of 30 subjects across two sites using Philips MRI systems (Philips Healthcare, Best, the Netherlands). All subjects provided written informed consent, and data collection complied with institutional and ethical guidelines. Table 1 summarizes the description of the cohort population and sites. The subjects were categorized into three age-groups: 11 young subjects (29 ± 4 years), 7 middle-aged (mid) subjects (63 ± 9 years), and 12 elderly subjects (82 ± 6 years). Eleven elderly subjects were previously diagnosed with aortic stenosis (AS).

Table 1: Age-group description across the cohort.

Group	Age [years]	Male / Female	Field strength	Pathology
Young	29 ± 4	5 / 6	1.5T	Healthy
Mid-age	63 ± 9	5 / 2	1.5T (3); 3T (4)	Healthy

Elderly	82 ± 6	9 / 3	3T	Aortic stenosis (11), Healthy (1)
---------	--------	-------	----	--------------------------------------

For each subject six to nine cine 2D MRI slices using either bSSFP or GRE were acquired approximately perpendicular to the aortic arch, using the MRI survey scan for planning. Image acquisition parameters were: 1.17-1.5 mm² in-plane resolution, 5-8 mm slice thickness and 25 ms temporal resolution (reconstructed to 40 temporal frames). The cine 2D slices were obtained evenly distributed across the arch, starting from one diameter upstream the sinotubular junction to the beginning of the abdominal aorta, with acquisitions acquired during individual breath-holds. In a subgroup of 10 subjects (3 young, 1 mid, 6 elderly; mean age 62 ± 23 years; 2 female), additional 4D flow MRI was acquired with 2.5 mm³ isotropic spatial and 50 ms temporal resolution. Data acquisition involved prospectively ECG gated phase-encoding with continuous acquisition followed by retrospective re-binning of data in reconstruction, to account for heart rate variability, and using a pseudo-spiral Cartesian undersampling scheme (acceleration factor $R = 4-6.7$), with repeated sampling of $k_y = k_z = 0$ profiles. At 3T, data were collected using a 13-point velocity encoding (venc) scheme with venc settings of 50/250 cm/s for healthy ($N = 3$) and 150/350 cm/s for aortic stenosed subjects ($N = 4$). At 1.5T, data were acquired with a 4-point scheme using a venc of 150 cm/s in all directions. All datasets were reconstructed with a locally-low-rank approach [34] and multi-venc acquisitions were combined using Bayesian unfolding [35] and retaining only the expiratory state for analysis. Peak systolic vessel segmentations were performed manually and with multiple iterative refinements over several days using ITK-SNAP [36].

2.4 Shape fitting evaluation

2.4.1 Synthetic data

The accuracy of the shape-fitting model was evaluated using 30 aortic meshes sampled from the statistical shape model with a standard deviation of $\sigma = 1.58$ around the mean shape (Figure 1A). For each geometry, a centerline was extracted and interpolated using cubic B-splines (SciPy implementation [31]). Using the Euclidean length of each centerline, twelve orthogonal cross-sections were generated along the aortic arch at uniform intervals of 1.3-1.8 cm, depending on the total aortic length and approximating the mean radius. Because the aortic root was excluded from the original statistical shape model, the mesh inlet corresponded to the sinotubular junction (STJ). For numerical stability during mesh intersection, the first cross-section was positioned 2.5 cm (approximately one aortic diameter) distal to the mesh's inlet. Subsequent cross-sections were then placed at uniform radial intervals along the arch. The second intersection coincided with the pulmonary artery (PA) plane, which is commonly used in clinical 2D flow MRI. This PA level (grey points indicated in Figure 1C) was therefore defined as the reference slice, encompassing intersections of both the ascending and descending aorta.

The influence of the number and position of intersected cross-sections on the accuracy of 3D shape reconstruction was then evaluated. Reconstruction accuracy was quantified using the Dice score (DSC), Intersection over Union (IoU), Hausdorff distance (HD), Chamfer distance, and relative radius errors computed at each of the 12 cross-sections along the centerline. A list of all utilized distance metrics and definitions is outlined in the Appendix.

An iterative slice-selection strategy was implemented, starting from the reference plane (PA level with slice positions 2 and 12) and progressively adding slices throughout the arch. At each iteration, the next slice position was chosen based on the lowest average distance error across all metrics. The process continued until all 12 cross-sections were incorporated. The resulting order of selection reflects the relative importance of each cross-section in reconstructing the

global shape, with slices selected earlier contributing more significantly to the overall reconstruction accuracy.

The aortic centerline used for slice placement was interpolated using cubic B-splines, which required at least five control points. Therefore, when fewer than five cross-sections were available, a surrogate centerline was estimated by fitting a semicircle between the first and last slices using their average radius as curvature. Finally, the model's ability to interpolate between sparsely sampled slices was further evaluated by computing relative radius errors - compared to the original geometries - at each of the 12 cross-sections for an increasing number of acquisition slices, using the optimal slice positions determined at each iteration.

2.4.2 *In-vivo* data

To evaluate voxel- and point-based accuracy, Dice scores, Intersection over Union, as well as Hausdorff- and Chamfer distances were computed between fitted peak systolic shapes and manually segmented 4D flow MRI data. For Dice score calculation, the fitted mesh was projected onto the 4D flow grid, while a smooth surface was generated from the 4D flow segmentations to compute distance metrics. Similar to the in-silico analysis, the relative radius errors were computed along the centerline. To correct for inter-scan motion relative to the cine 2D MRI slices, the volumetric masks were visually inspected and manually adjusted when needed using minor rigid translations.

2.5 In-plane vessel segmentation

Initial coarse aortic segmentations were obtained from the standard MRI survey scan in axial direction using a conventional U-Net [37]. The segmented volume was skeletonized (using Scikit-learn) and fitted using a B-spline to extract the vessel centerline. This centerline was subsequently intersected with the cine 2D MRI slices to localize the aorta in the 2D slices, enabling cropping to 64×64 in-plane regions-of-interest. The nnU-Net [38] was trained to segment the aorta in the cropped cine 2D MRI images. For network training we utilized 22 subjects (healthy and stenosed), for which multiple acquisitions were available, resulting in a total of 150 datasets. Segmentation performance was evaluated on an independent test set comprising eight healthy subjects (mean age: 48 ± 22 years; 3 female), scanned on the same 3T system. To minimize inter-scanner variability given the limited dataset size, the test set was restricted to acquisitions from a single scanner. In addition, four elderly stenosed subjects were exchanged with younger healthy volunteers to enable a publicly shareable test dataset and assess segmentation performance on a broader age range. To evaluate breath-hold position misalignments, we evaluated overlap between three subsequent breath-holds for each test subject. Evaluation metrics included temporal Dice score, Intersection over Union, Hausdorff distance and Average surface distance (ASD).

2.6 Vessel metrics

After shape fitting, aortic shape features were computed, as described in [16]. Each shape was orthogonally sliced along its centerline in 7.5 mm intervals (Figure 1C). As illustrated in Figure 1C, the aorta was anatomically divided into three regions: ascending (A-B), arch-top (B-T-C) and descending (C-D). Geometric parameters including arch height (h), arch width (w) and centerline lengths were extracted. Aortic tortuosity was defined as $T = 1 - \frac{w}{L-AD}$, where $L-AD$ is the centerline length from the ascending to the descending aorta.

Wall motion was quantified as the norm of the distance of mesh cell centers, calculated as the distance $d(p_0, p_t)$ between different cardiac phases p_t (with time index t) and the diastolic reference state p_0 . Relative radial vessel wall strains were evaluated as $\varepsilon = \frac{\Delta r}{r_0}$ with $\Delta r = |r_t -$

$r_0|$, where r_t and r_0 represent vessel radii at systolic phase t and diastolic phase t_0 , respectively. Maximum average strain values along the ascending aorta and maximum centerline extensions within L-AD were computed.

The distributions of all shape, strain, and centerline parameters were examined for normality and equality of variances within each age group. Based on these assessments, pairwise group comparisons were performed using either Student's t-test when variances were similar or Welch's t-test when variances differed.

3 Results

3.1 Shape fitting evaluation

3.1.1 Synthetic data

For each combination of slices placed between positions 2 and 12 (see inset in Figure 3), we computed the Dice score, Intersection over Union, Hausdorff distance and Chamfer distance. Figure 3 illustrates how the number and positioning of slices affect the accuracy of the shape fitting process. The horizontal axis shows all candidate positions, sorted by the next optimal slice, while the vertical axis indicates the number of in-silico “acquired” slices. At each iteration, the mean of all metrics was calculated, and the best-performing case (highlighted along the diagonal) was selected for the next iteration. Notably, slice position 1 was only considered after the first iteration. A mean \pm standard deviation in Dice score of $(94.8 \pm 1.1) \%$, Intersection over Union of $(90.1 \pm 2.0) \%$, Hausdorff distance of $(5.9 \pm 2.3) \text{ mm}$ and Chamfer distance of $(2.5 \pm 0.4) \text{ mm}$ was achieved when including the 6th slice, as highlighted in red. Iteratively applying this selection strategy resulted in a final Dice score of $(96.7 \pm 0.3) \%$, Intersection over Union of $(93.5 \pm 0.5) \%$, Hausdorff- and Chamfer distances of $(4.5 \pm 1.7) \text{ mm}$ and $(2.0 \pm 0.2) \text{ mm}$, respectively.

Radius error calculations were performed across the twelve cross-sections along the centerline for an increasing number of slices included in the shape reconstruction, referenced against the original shape. Results show a progressive reduction in relative radius errors with each iteration, see Figure 4, with only minor improvements from 7 slices upwards. Specifically, the total mean (μ) and standard deviation (σ) of relative errors for six and eleven slices were $(0.2 \pm 1.1) \times 10^{-1}$ and $(-0.2 \pm 1.2) \times 10^{-3}$, respectively. Corresponding mean radius errors were found as $(0.32 \pm 1.70) \text{ mm}$ for six acquisition slices and $(0.03 \pm 0.17) \text{ mm}$ for eleven acquisition slices.

3.1.2 In-vivo data

Evaluation against manually segmented 4D flow MRI data showed agreement between the fitted shapes and reference ones. A mean Dice score of $(89.9 \pm 1.6) \%$, Intersection over Union of $(81.7 \pm 2.7) \%$, Hausdorff distance of $(7.3 \pm 3.3) \text{ mm}$ and Chamfer distance of $(3.7 \pm 0.6) \text{ mm}$ were calculated. Additionally, the analysis of relative radius errors based on uniformly spaced cross-sectional slices along the centerline resulted in an absolute radius error of $(0.8 \pm 0.6) \text{ mm}$, and a relative error of $(3 \pm 7) \times 10^{-2}$, demonstrating high shape fidelity throughout.

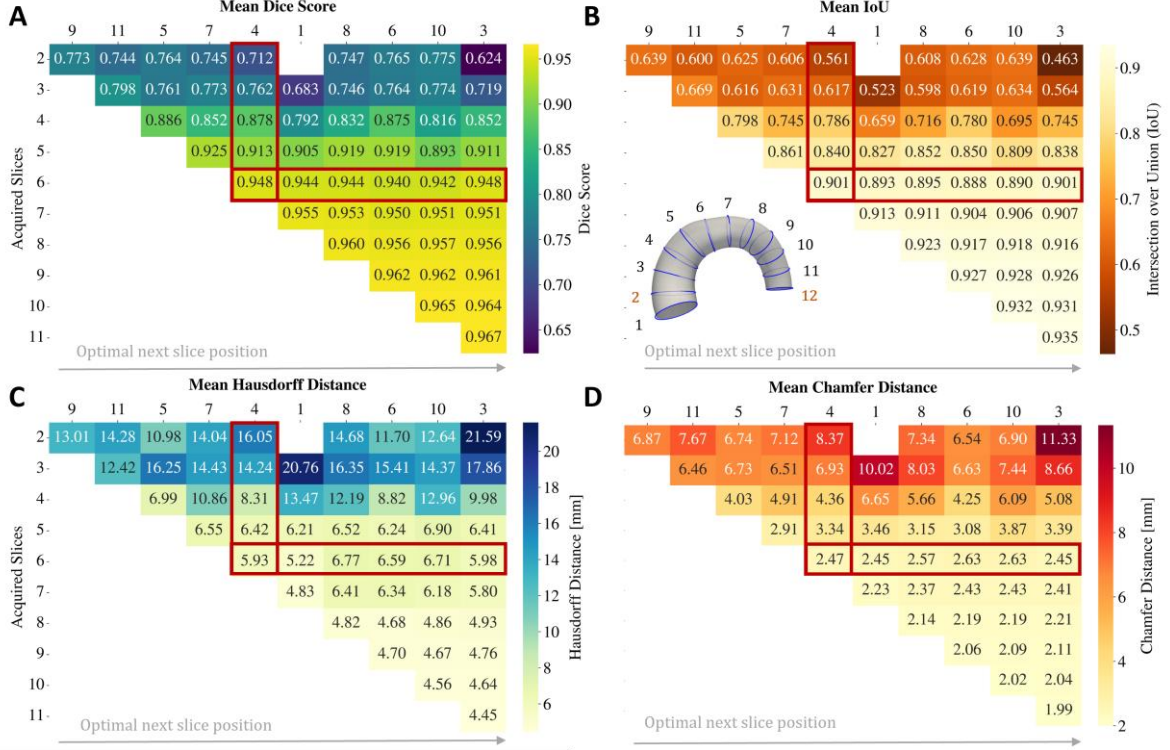


Figure 3: Impact of slice number and positioning on mean Dice scores (A) and Intersection over Union (B), Hausdorff distance (C) and Chamfer distance (D) with the number of acquired slices and optimal next slice positions denoted along the vertical and horizontal axes, respectively. The slices yielding the highest mean metric were selected for the following iteration (diagonal). Red boxes highlight the desired Dice score of 95 %, with IoU 90 %, average Hausdorff distance at 6 mm and average Chamfer distance at 2.5 mm, when including 6 slices.

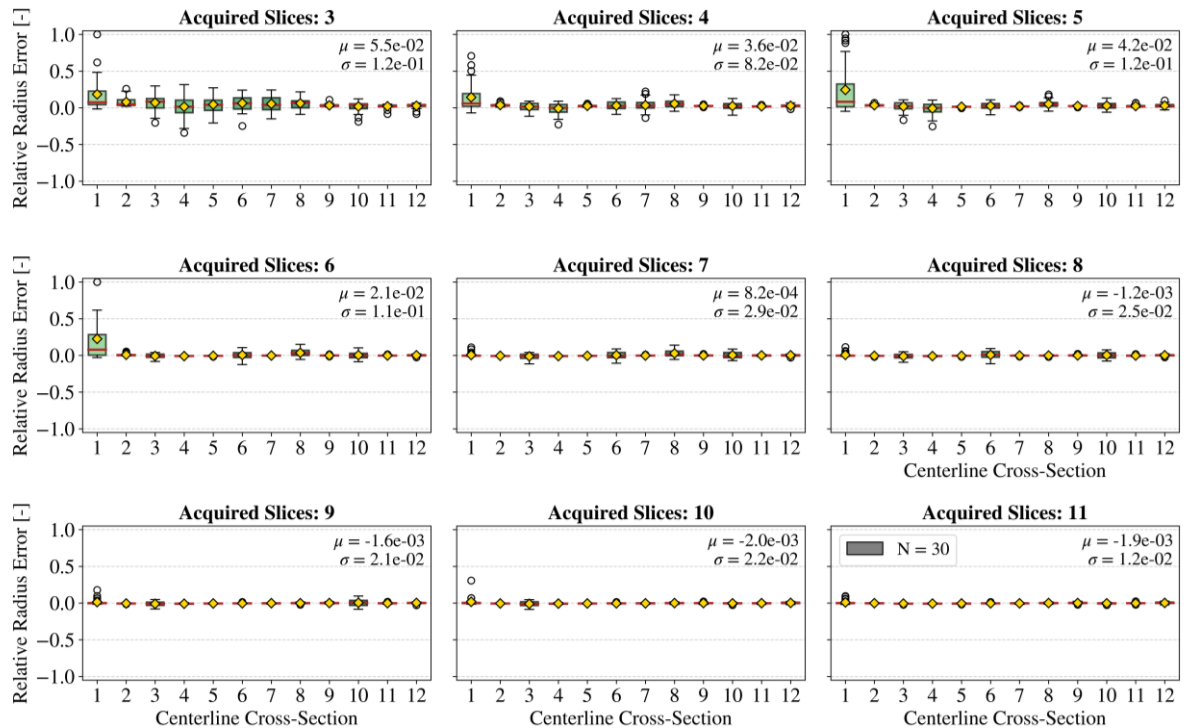


Figure 4: Relative radius errors for increasing number of acquired slices. The relative radius errors of cross-sectional slices along the centerline are plotted for an increasing number of “acquired” slices. Resulting total mean relative errors for six and eleven slices were found as $(0.2 \pm 1.1) \times 10^{-1}$ and $(-0.2 \pm 1.2) \times 10^{-3}$, respectively.

3.2 In-plane vessel segmentation

The nnU-Net model achieved high segmentation accuracy for both, the ascending and descending aorta (see Appendix Figure A1). Table 2 summarizes the quantitative comparison of predicted segmentations against reference masks, reporting temporal averaged Dice scores, Intersection over Union, Hausdorff distance and average surface distance for ascending (AAo) and descending (DA) aorta, as well as the evaluation of averaged metrics from the three individual breath-holds as predicted by the network, referred to as MultiB-AAo and MultiB-DA.

Table 2: Global distance metrics on the test dataset for ascending (AAo) and descending (DA) aorta with comparison between multiple breath-holds (MultiB) based on the network predictions.

Data	DSC \uparrow	IoU \uparrow	HD [mm] \downarrow	ASD [mm] \downarrow
AAo	0.965 ± 0.012	0.933 ± 0.022	2.01 ± 0.30	0.20 ± 0.08
MultiB-AAo	0.957 ± 0.024	0.918 ± 0.042	2.03 ± 0.71	0.24 ± 0.11
DA	0.944 ± 0.023	0.894 ± 0.040	1.87 ± 0.36	0.26 ± 0.11
MultiB-DA	0.950 ± 0.025	0.907 ± 0.045	2.13 ± 2.14	0.22 ± 0.10

3.3 Vessel metrics

3.3.1 Shape feature analysis

The comparison of shape features across age-groups (young vs. middle-age vs. elderly) is presented in Figure 5. An increase in aortic size with age was measured in radii parameters for ascending (A): (11.1 ± 1.2) mm vs. (15.3 ± 0.9) mm vs. (16.6 ± 1.1) mm, top (B): (9.3 ± 1.2) mm vs. (12.2 ± 0.8) mm vs. (13.7 ± 1.1) mm, and descending (C): (8.4 ± 1.0) mm vs. (11.2 ± 0.8) mm vs. (12.5 ± 0.8) mm, respectively. In addition, ascending (D) and total (E) aortic arch lengths increased from (58.3 ± 9.6) and 120.9 ± 17.6 mm in the young vs. (77.8 ± 11.3) and 156.9 ± 15.2 mm in the intermediate vs. (97.3 ± 13.9) and 189.7 ± 27.7 mm in the elderly group. Aortic arch widths (F) and heights (G) also increased with age: (53.0 ± 5.7) mm vs. (73.4 ± 6.3) mm vs. (94.1 ± 11.2) mm and (45.8 ± 7.8) mm vs. (56.0 ± 6.9) mm vs. (65.2 ± 10.3) mm, respectively. Statistical testing revealed strong age-related differences ($p < 0.001$) between the young and elderly group for all parameters except tortuosity ($p < 0.05$).

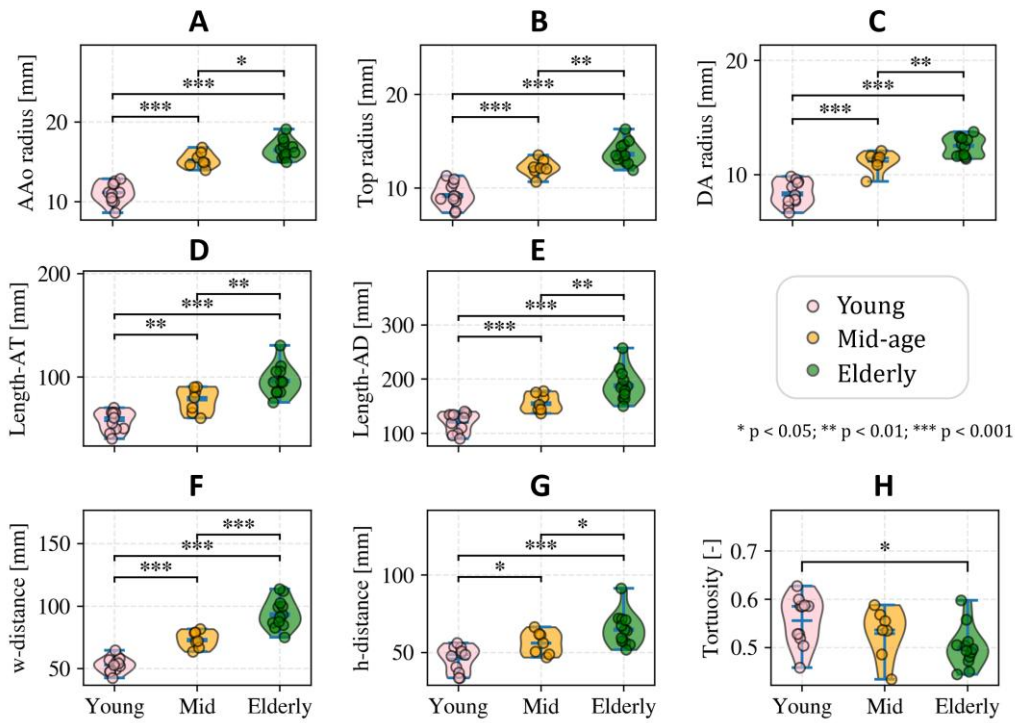


Figure 5: Aortic shape feature comparison across age groups. Violin plots displaying the distribution of aortic shape features (ascending aortic (AAo), top (Top) and descending aortic (DA) radii (A-C), ascending (D) and total (E) aortic arch length, width (F), height (G) and tortuosity (H)) in young, mid-age, and elderly subjects. Significant increases in size were observed with age, with the largest differences between young and elderly groups ($p < 0.001$), except for tortuosity ($p < 0.05$).

3.3.2 Wall deformation and strains

Figure 6A illustrates relative wall motion across the three age groups (young, mid-age, elderly) in two examples for peak systole relative to end diastole. Peak systolic radial strains, averaged across the ascending aortic arch, are compared in Figure 6B. The data shows significant difference ($p < 0.001$) in radial strains between the young vs. mid-age and young vs. elderly groups, with mean and standard deviation values of $(11.00 \pm 3.11) \times 10^{-2}$ vs. $(3.74 \pm 1.25) \times 10^{-2}$ vs. $(2.89 \pm 0.87) \times 10^{-2}$, respectively. Relative aortic centerline length change between diastole and peak systole were $(3.5 \pm 1.0) \%$ vs. $(1.9 \pm 0.4) \%$ vs. $(1.4 \pm 0.4) \%$ with largest difference ($p < 0.001$) between young and elderly.

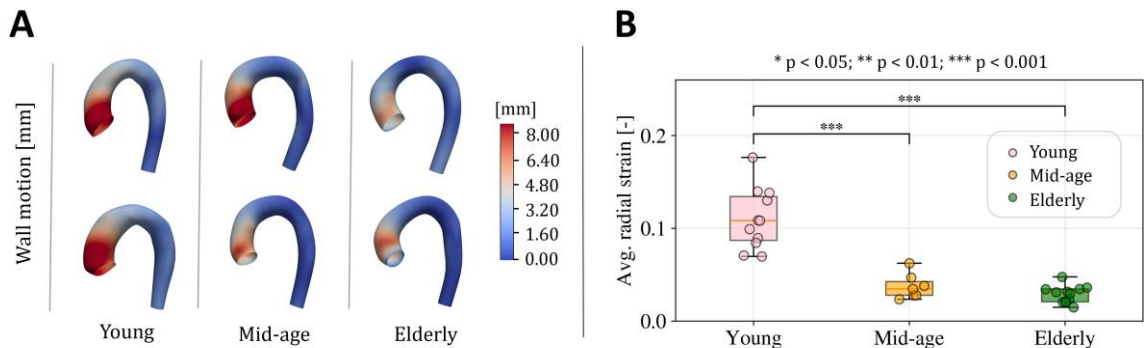


Figure 6: Wall motion maps and radial strain analysis. (A) Wall motion across three age groups (young, mid-age, elderly) is illustrated with two examples each at peak systole. (B) Peak systolic radial wall strains, averaged across the ascending aortic arch.

4 Discussion

A method for generating time-resolved, three-dimensional aortic meshes from a limited number of cine 2D MRI slices has been presented. Compared to 4D flow MRI data, the approach benefits from superior in-plane spatial and temporal resolution, leveraging the high image quality of standard 2D MRI acquisitions. We have demonstrated that accurate 3D aortic geometries can be obtained from as few as six uniformly distributed slices along the aortic arch.

For differentiable volumetric mesh optimization, we employed an asymmetric Chamfer distance loss (referred to as “mesh loss”), to balance accurate warping with realistic shape convergence. In addition, we introduced a centerline loss, which proved essential for fast convergence. Training parameters, such as epoch count and learning rate, were optimized via grid search to ensure reconstruction accuracy and computational efficiency. Analysis indicated that six acquisition slices were sufficient to achieve fitting errors markedly below the imaging resolution.

The shapes derived from 2D MRI slices showed good agreement with shapes derived from 4D flow MRI obtained in a subset of subjects, comparing favorably with previously reported Dice scores of 0.83 to 0.92 [26–29]. While 4D flow MRI has inherent limitations in spatial resolution and vessel-to-background contrast, it was used here as a pragmatic volumetric reference for peak-systolic geometry comparison rather than as an absolute ground truth. In comparison to [30], we found slightly lower Dice agreement, likely due to differences in spatial resolution between scans and additional partial-volume effects during mesh-to-voxel sampling. Chamfer distances remained close to the image resolution, while vessel radius errors were consistently lower than image resolution throughout the entire arch.

Although age and disease effects cannot be separated in the present cohort, the observed trends are consistent with previously reported age-associated anatomical changes [5, 6, 16], demonstrating the framework’s ability to reconstruct geometries across a heterogenous age spectrum within the studied cohort. Older subjects exhibited significantly larger aortic radii, longer centerlines, and increased arch heights and widths, as seen in literature. Time-resolved shape analysis enabled automatic estimation of wall motion, revealing reduced displacement, lower radial strain and relative centerline length change with increasing age, which is expected due to progressive aortic stiffening [7]. The nnU-Net-based segmentation demonstrated high temporal accuracy in both ascending and descending aortic cross-sections, (Dice scores > 94 %) with strong agreement to reference annotations, supporting the feasibility of automated, high-fidelity vessel segmentation. This is in line with previous applications of the nnU-Net trained on volumetric aortic MRIs [30, 39] and with previous traditional- and machine learning derived approaches segmenting aortic cine 2D MRI slices [40, 41].

The proposed approach has several limitations. The statistical shape model was not evaluated on pathological anatomies such as aortic coarctations or dissections, which limits its immediate applicability to certain disease populations. While the combination of multiple 2D cine MRI slices provides a time-efficient alternative to full 4D flow MRI acquisitions, it may be affected by patient motion in-between scans, which can increase shape uncertainty. While we showed that in our dataset slice positioning was consistent, this is usually not guaranteed in clinical applications. Further, the current framework does not include the aortic root, despite its known relevance in valvular pathologies such as aortic stenosis. While technically feasible, extending the model to include the root, either through direct anatomical modelling or integration of established root-specific shape models [42, 43] remains to be explored and validated, particularly in diseased populations [44]. Additionally, the elderly subgroup predominantly consisted of subjects with aortic stenosis, which limits the ability to disentangle

age-related from disease-specific remodelling effects. Accordingly, the presented group differences should not be interpreted as isolated effects of physiological aging. Larger, pathology-stratified and age-matched cohorts will be required to separately characterize aging and disease contributions. Moreover, given the limited size of available datasets, the nnU-Net was employed solely to evaluate the feasibility of automatic cross-sectional slice segmentation in support of the rapid shape reconstruction pipeline. All contours used for generating the personalized, time-resolved aortic geometries were derived from manually annotated data. In addition, the nnU-Net was trained and evaluated within the same study cohort and primarily on data from a single scanner vendor. Therefore, direct generalization to other vendors and field strengths can not be guaranteed and remain subject to future investigation.

5 Conclusion

A method for generating time-resolved, patient-specific aortic geometries from a limited number of standard cine 2D MRI slices enables efficient extraction of dynamic 3D meshes suitable for shape and strain analyses.

Data availability

Our Python code for generating time-resolved subject-specific shape models from cine 2D MRI data is available on: https://gitlab.ethz.ch/ibt-cmr/publications/Temporal_Aortic_Shape_Twining/.

Declaration of competing interest

The authors declare that they have no known competing financial interests or personal relationships that could have appeared to influence the work reported in this paper.

Acknowledgements

The authors acknowledge funding from the Swiss National Science Foundation (SNSF), grant CR23I3_166485, a Microsoft Joint Swiss Research grant and support from the Swiss Heart Foundation.

Glossary (alphabetical)

- Ascending aorta (AAo)
- Average surface distance (ASD)
- Balanced-steady-state-free-precession (bSSFP)
- Computed Tomography (CT)
- Dice score (DSC)
- Descending aorta (DA)
- Gradient Echo (GRE)
- Hausdorff distance (HD)
- Intersection over Union (IoU)
- Magnetic Resonance Imaging (MRI)
- Principal Component Analysis (PCA)
- Radial basis function (RBF)
- Statistical shape model (SSM)

CRedit author statement

Gloria Wolkerstorfer: Conceptualization, Methodology, Software, Validation, Formal analysis, Investigation, Data Curation, Writing Original Draft, Writing Review Editing, Visualization;

Stefano Buoso: Conceptualization, Methodology, Writing Original Draft, Writing Review Editing, Supervision; **Rabea Schlenker:** Resources, Writing Review Editing; **Jochen von Spiczak:** Writing Review Editing; **Robert Manka:** Writing Review Editing, **Sebastian Kozerke:** Conceptualization, Methodology, Writing Original Draft, Writing Review Editing, Supervision, Project administration, Funding acquisition.

AI use declaration:

During the preparation of this work the authors used ChatGPT for spellchecking and to improve the clarity of text. After using this tool, the authors reviewed and edited the content as needed and take full responsibility for the content of the publication.

Appendix

A.1 In-plane vessel segmentation analysis

Figure A1 illustrates temporal segmentation performance of the nnU-Net on the test subjects, with Dice scores of AAo and DA outlined in panel A. Predicted versus reference aortic radii at peak systole and one diastolic frame were compared using linear regression (panel B) and Bland-Altman analysis (panel C), which shows strong agreement between predicted to reference mask's radii.

For the ascending aorta, the regression equation was $y = 0.93x + 0.90$ with r value of 0.98, a mean bias of -0.21 mm, confidence interval (CI) of [-0.45, 0.04] mm, and limits of agreement (LoA) of [-1.19, 0.78] mm. For the descending aorta, the results were $y = 0.90x + 0.9$, $r = 0.95$, with a mean bias of -0.46 mm, CI of [-0.75, -0.16] mm, and LoAs of [-1.64, 0.73] mm.

Repeatability analysis was conducted comparing segmentations predictions against reference segmentations from two annotators. Table A1 outlines global distance metrics between the initial reference annotation (R1 - as used in the manuscript) vs. second annotator (R2) vs. network predictions (P). Best segmentation agreement was found between the second annotator (R2) and network prediction, which we attribute to the expert's experience.

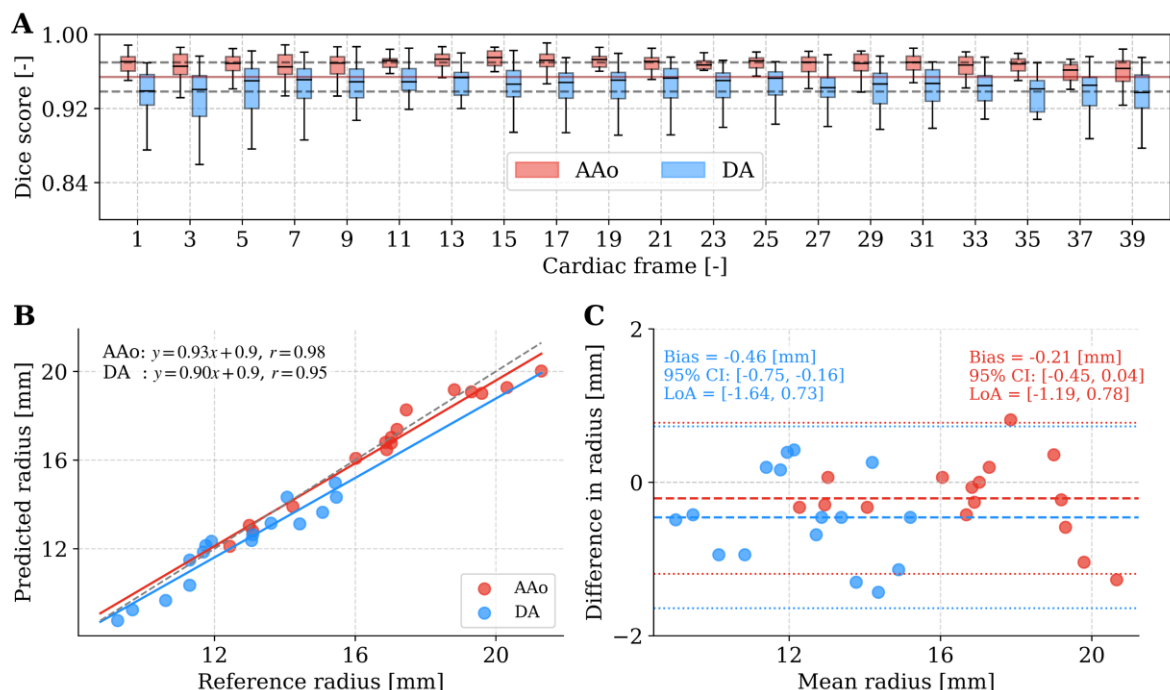


Figure A1: Segmentation performance of the nnU-Net. (A) Temporal Dice scores in ascending (AAo in red) and descending (DA in blue) aorta across the cardiac cycle, for every interleaved frame. (B) Regression and (C) Bland-

Altman analyses of radii at peak systolic and diastolic frame indicate strong agreement with manual annotations with displayed bias, confidence interval (CI), and limits of agreement (LoA) for AAo and DA, respectively.

Table A1: Global distance metrics between initial segmentation (R1) vs. second annotator (R2) and network predictions (P), for ascending (AAo) and descending aorta (DA), respectively.

Data	DSC \uparrow	IoU \uparrow	HD [mm] \downarrow	ASD [mm] \downarrow
AAo (R₁ vs. P)	0.965 ± 0.012	0.933 ± 0.022	2.01 ± 0.30	0.20 ± 0.08
AAo (R₂ vs. P)	0.972 ± 0.003	0.946 ± 0.006	1.77 ± 0.36	0.16 ± 0.02
AAo (R₁ vs. R₂)	0.964 ± 0.007	0.930 ± 0.013	2.30 ± 0.29	0.20 ± 0.33
DA (R₁ vs. P)	0.944 ± 0.023	0.894 ± 0.040	1.87 ± 0.36	0.26 ± 0.11
DA (R₂ vs. P)	0.960 ± 0.011	0.923 ± 0.021	1.87 ± 0.62	0.19 ± 0.06
DA (R₁ vs. R₂)	0.948 ± 0.025	0.903 ± 0.043	1.84 ± 0.79	0.24 ± 0.12

A.2 Statistical Analysis

To quantify the performance of binary segmentation masks, the number of true positives (TP), false positives (FP), true negatives (TN), and false negatives (FN) was used to compute the following voxel-wise metrics:

- Dice Score (DSC) quantifies the spatial overlap between predicted and reference segmentations:

$$\text{Dice} = \frac{2TP}{2TP + FP + FN}$$

ranging from 0 (no overlap) to 1 (perfect agreement).

- Intersection over Union (IoU) measures the ratio of the intersection to union:

$$\text{IoU} = \frac{TP}{TP + FP + FN}$$

also ranging 0 to 1, with stronger penalization for mismatches.

For surface-based evaluation, let X and Y denote the sets of boundary points extracted from the predicted and reference segmentations, respectively, with $d(x, y)$ defined as the Euclidean distance between points. Then the following point-set metrics can be defined:

- The Hausdorff Distance (HD) quantifies the maximum surface discrepancy:

$$\text{HD}(X, Y) = \max(h(X, Y), h(Y, X)),$$

where $h(A, B)$ is given by

$$h(A, B) = \max_{a \in A} \left(\min_{b \in B} (d(a, b)) \right).$$

- The Average Surface Distance (ASD) quantifies the mean bi-directional surface discrepancy as:

$$\text{ASD}(X, Y) = \frac{1}{|X| + |Y|} \left(\sum_{x \in X} \min_{y \in Y} d(x, y) + \sum_{y \in Y} \min_{x \in X} (d(x, y)) \right),$$

and is less sensitive to outliers than the HD.

- The Chamfer Distance (CD) quantifies the mean bi-directional surface discrepancy as:

$$CD(X, Y) = \frac{1}{|X|} \sum_{x \in X} \min_{y \in Y} d(x, y) + \frac{1}{|Y|} \sum_{y \in Y} \min_{x \in X} (d(x, y)),$$

which is similar to the ASD, but with different normalization.

References

1. Sel, K., Osman, D., Zare, F., Masoumi Shahrababak, S., Brattain, L., Hahn, J.O., Inan, O.T., Mukkamala, R., Palmer, J., Paydarfar, D., Pettigrew, R.I., Quyyumi, A.A., Telfer, B., Jafari, R. (2024). Building Digital Twins for Cardiovascular Health: From Principles to Clinical Impact. *Journal of the American Heart Association*, 13(19): e031981. <https://doi.org/10.1161/JAHA.123.031981>
2. Niederer, S.A., Sacks, M.S., Girolami, M., Willcox, K. (2021). Scaling digital twins from the artisanal to the industrial. *Nature Computational Science*, 1(5): 313–320. <https://doi.org/10.1038/s43588-021-00072-5>
3. Viola, F., Del Corso, G., De Paulis, R., Verzicco, R. (2023). GPU accelerated digital twins of the human heart open new routes for cardiovascular research. *Scientific Reports*, 13: 34098. <https://doi.org/10.1038/s41598-023-34098-8>
4. Callaghan, F.M., Bannon, P., Barin, E., Celemajer, D., Jeremy, R., Figtree, G., Grieve, S.M. (2019). Age-related changes of shape and flow dynamics in healthy adult aortas: A 4D flow MRI study. *Journal of Magnetic Resonance Imaging*, 49(1): 90–100. <https://doi.org/10.1002/jmri.26210>
5. Komutrattananont, P., Mahakkanukrauh, P., Das, S. (2019). Morphology of the human aorta and age-related changes: anatomical facts. *Anatomy & Cell Biology*, 52(2): 109–114. <https://doi.org/10.5115/acb.2019.52.2.109>
6. Redheuil, A., Yu, W.C., Mousseaux, E., Harouni, A.A., Kachenoura, N., Wu, C.O., Bluemke, D., Lima, J.A.C. (2011). Age-Related Changes in Aortic Arch Geometry: Relationship With Proximal Aortic Function and Left Ventricular Mass and Remodeling. *Journal of the American College of Cardiology*, 58(12): 1262–1270. <https://doi.org/10.1016/j.jacc.2011.06.012>
7. Craiem, D., Chironi, G., Redheuil, A., Casciaro, M., Mousseaux, E., Simon, A., Armentano, R.L. (2012). Aging impact on thoracic aorta 3D morphometry in intermediate-risk subjects: Looking beyond coronary arteries with non-contrast cardiac CT. *Annals of Biomedical Engineering*, 40(5): 1028–1038. <https://doi.org/10.1007/s10439-011-0487-y>
8. Bruse, J.L., Zuluaga, M.A., Khushnood, A., McLeod, K., Ntsinjana, H.N., Hsia, T.Y., Sermesant, M., Pennec, X., Taylor, A.M., Schievano, S. (2017). Detecting Clinically Meaningful Shape Clusters in Medical Image Data: Metrics Analysis for Hierarchical Clustering Applied to Healthy and Pathological Aortic Arches. *IEEE Transactions on Biomedical Engineering*, 64(10): 2373–2383. <https://doi.org/10.1109/TBME.2017.2655364>
9. Cosentino, F., Raffa, G.M., Gentile, G., Agnese, V., Bellavia, D., Pilato, M., Pasta, S. (2020). Statistical Shape Analysis of Ascending Thoracic Aortic Aneurysm: Correlation between Shape and Biomechanical Descriptors. *Journal of Personalized Medicine*, 10(2): 28. <https://doi.org/10.3390/jpm10020028>
10. Dietenbeck, T., Bouaou, K., Houriez-Gombaud-Saintonge, S., Guo, J., Gencer, U., Charpentier, E., Giron, A., De Cesare, A., Nguyen, V., Gallo, A., Boussouar, S., Pasi, N., Soulat, G., Redheuil, A., Mousseaux, E., Kachenoura, N. (2023). Value of aortic volumes assessed by automated segmentation of 3D MRI data in patients with thoracic aortic

dilatation: A case-control study. *Diagnostic and Interventional Imaging*, 104(4): 419–426. <https://doi.org/10.1016/j.diii.2023.04.004>

11. Lenz, A., Binter, C., Semaan, E., Kozerke, S. (2020). 4D flow cardiovascular magnetic resonance for monitoring of aortic valve repair and changes in blood flow dynamics. *Journal of Cardiovascular Magnetic Resonance*, 22(1): 56. <https://doi.org/10.1186/s12968-020-00608-0>
12. Dirix, P., Jacobs, L., Buoso, S., Kozerke, S. (2025). Synthesizing Scalable CFD-Enhanced Aortic 4D Flow MRI for Assessing Accuracy and Precision of Deep-Learning Image Reconstruction and Segmentation Tasks. In *Lecture Notes in Computer Science*, Vol. 15187 LNCS, pp. 157–166. https://doi.org/10.1007/978-3-031-73281-2_15
13. Rouhollahi, A., Willi, J.N., Haltmeier, S., Mehrtash, A., Straughan, R., Javadikasgari, H., Brown, J., Itoh, A., de la Cruz, K.I., Aikawa, E., Edelman, E.R., Nezami, F.R. (2023). CardioVision: A fully automated deep learning package for medical image segmentation and reconstruction generating digital twins for patients with aortic stenosis. *Computerized Medical Imaging and Graphics*, 109: 102289. <https://doi.org/10.1016/j.compmedimag.2023.102289>
14. Bruse, J.L., McLeod, K., Biglino, G., Ntsinjana, H.N., Capelli, C., Hsia, T.Y., Sermesant, M., Pennec, X., Taylor, A.M., Schievano, S., Taylor, A., Giardini, A., Khambadkone, S., de Leval, M., Bove, E., Dorfman, A., Baker, G.H., Hlavacek, A., Migliavacca, F., Pennati, G., Dubini, G., Marsden, A., Vignon-Clementel, I., Figliola, R., McGregor, J. (2016). A statistical shape modelling framework to extract 3D shape biomarkers from medical imaging data: Assessing arch morphology of repaired coarctation of the aorta. *BMC Medical Imaging*, 16: 42. <https://doi.org/10.1186/s12880-016-0142-z>
15. Thamsen, B., Yevtushenko, P., Gundelwein, L., Setio, A.A.A., Lamecker, H., Kelm, M., Schafstedde, M., Heimann, T., Kuehne, T., Goubergrits, L. (2021). Synthetic Database of Aortic Morphometry and Hemodynamics: Overcoming Medical Imaging Data Availability. *IEEE Transactions on Medical Imaging*, 40(5): 1438–1449. <https://doi.org/10.1109/TMI.2021.3057496>
16. Romero, P., Lozano, M., Martínez-Gil, F., Serra, D., Sebastián, R., Lamata, P., García-Fernández, I. (2021). Clinically-Driven Virtual Patient Cohorts Generation: An Application to Aorta. *Frontiers in Physiology*, 12: 713118. <https://doi.org/10.3389/fphys.2021.713118>
17. Joyce, T., Buoso, S., Stoeck, C.T., Kozerke, S. (2022). Rapid inference of personalised left-ventricular meshes by deformation-based differentiable mesh voxelization. *Medical Image Analysis*, 79: 102445. <https://doi.org/10.1016/j.media.2022.102445>
18. Dillon, J.R., Mauger, C., Zhao, D., Petersen, S.E., McCulloch, A.D., Young, A.A., Nash, M.P. (2025). An Open-Source End-to-End Pipeline for Generating 3D+t Biventricular Meshes from Cardiac Magnetic Resonance Imaging. In *Functional Imaging and Modeling of the Heart – 13th Int. Conf. (FIMH 2025), Lecture Notes in Computer Science*, Vol. 15673, pp. 372–383. https://doi.org/10.1007/978-3-031-94562-5_34
19. Kramer, C.M., Barkhausen, J., Bucciarelli-Ducci, C., Flamm, S.D., Kim, R.J., Nagel, E. (2020). Standardized cardiovascular magnetic resonance imaging (CMR) protocols: 2020 update. *Journal of Cardiovascular Magnetic Resonance*, 22: 17. <https://doi.org/10.1186/s12968-020-00607-1>

20. Dyverfeldt, P., Bissell, M., Barker, A.J., Bolger, A.F., Carlhäll, C.J., Ebbers, T., Francois, C.J., Frydrychowicz, A., Geiger, J., Giese, D., Hope, M.D., Kilner, P.J., Kozerke, S., Myerson, S., Neubauer, S., Wieben, O., Markl, M. (2015). 4D flow cardiovascular magnetic resonance consensus statement. *Journal of Cardiovascular Magnetic Resonance*, 17: 72. <https://doi.org/10.1186/s12968-015-0174-5>
21. Markl, M., Frydrychowicz, A., Kozerke, S., Hope, M., Wieben, O. (2012). 4D flow MRI. *Journal of Magnetic Resonance Imaging*, 36(5): 1015–1036. <https://doi.org/10.1002/jmri.23632>
22. Garcia, J., Barker, A.J., Markl, M. (2019). The Role of Imaging of Flow Patterns by 4D Flow MRI in Aortic Stenosis. *JACC: Cardiovascular Imaging*, 12(2): 252–266. <https://doi.org/10.1016/j.jcmg.2018.10.034>
23. Bissell, M.M., Raimondi, F., Ait Ali, L., Allen, B.D., Barker, A.J., Bolger, A., Burris, N., Carlhäll, C.J., Collins, J.D., Ebbers, T., Francois, C.J., Frydrychowicz, A., Garg, P., Geiger, J., Ha, H., Hennemuth, A., Hope, M.D., Hsiao, A., Johnson, K., Kozerke, S., Ma, L.E., Markl, M., Martins, D., Messina, M., Oechtering, T.H., van Ooij, P., Rigsby, C., Rodriguez-Palomares, J., Roest, A.A.W., Roldán-Alzate, A., Schnell, S., Sotelo, J., Stuber, M., Syed, A.B., Töger, J., van der Geest, R., Westenberg, J., Zhong, L., Zhong, Y., Wieben, O., Dyverfeldt, P. (2023). 4D Flow cardiovascular magnetic resonance consensus statement: 2023 update. *Journal of Cardiovascular Magnetic Resonance*, 25: 25. <https://doi.org/10.1186/s12968-023-00942-z>
24. Bustamante, M., Viola, F., Engvall, J., Carlhäll, C., Ebbers, T. (2023). Automatic Time-Resolved Cardiovascular Segmentation of 4D Flow MRI Using Deep Learning. *Journal of Magnetic Resonance Imaging*, 51(1): 191–203. <https://doi.org/10.1002/jmri.28221>
25. Marin-Castrillon, D.M., Geronzi, L., Boucher, A., Lin, S., Morgant, M.-C., Cochet, A., Rochette, M., Leclerc, S., Ambarki, K., Jin, N., Aho, L.S., Lalande, A., Bouchot, O., Presles, B. (2023). Segmentation of the aorta in systolic phase from 4D flow MRI: multi-atlas vs. deep learning. *Magnetic Resonance Materials in Physics, Biology and Medicine*, 36(3): 687–700. <https://doi.org/10.1007/s10334-023-01066-2>
26. Garzia, S., Scarpolini, M.A., Mazzoli, M., Capellini, K., Monteleone, A., Cademartiri, F., Positano, V., Celi, S. (2023). Coupling synthetic and real-world data for a deep learning-based segmentation process of 4D flow MRI. *Computer Methods and Programs in Biomedicine*, 242: 107790. <https://doi.org/10.1016/j.cmpb.2023.107790>
27. Fujiwara, T., Berhane, H., Scott, M.B., Englund, E.K., Schäfer, M., Fonseca, B., Berthussen, A., Robinson, J.D., Rigsby, C.K., Browne, L.P., Markl, M., Barker, A.J. (2022). Segmentation of the Aorta and Pulmonary Arteries Based on 4D Flow MRI in the Pediatric Setting Using Fully Automated Multi-Site, Multi-Vendor, and Multi-Label Dense U-Net. *Journal of Magnetic Resonance Imaging*, 55(6): 1666–1680. <https://doi.org/10.1002/jmri.27995>
28. Manokaran, J., Flores, J.G., Ukwatta, E. (2023). Fully automated aortic segmentation of 3D phase-contrast magnetic resonance angiography images using deep learning techniques. *Proceedings of SPIE*, 12468: 31–37. <https://doi.org/10.1117/12.2653344>
29. Barrera-Naranjo, A., Marin-Castrillon, D.M., Decourselle, T., Lin, S., Leclerc, S., Morgant, M.C., Bernard, C., De Oliveira, S., Boucher, A., Presles, B., Bouchot, O., Christophe, J.J., Lalande, A. (2023). Segmentation of 4D Flow MRI: Comparison between 3D Deep

Learning and Velocity-Based Level Sets. *Journal of Imaging*, 9(6): 123.

<https://doi.org/10.3390/jimaging9060123>

30. Merton, R., Bosshardt, D., Strijkers, G.J., Nederveen, A.J., Schrauben, E.M., van Ooij, P. (2024). Assessing aortic motion with automated 3D cine balanced steady state free precession cardiovascular magnetic resonance segmentation. *Journal of Cardiovascular Magnetic Resonance*, 26: 101089. <https://doi.org/10.1016/j.jcmr.2024.101089>
31. Virtanen, P., Gommers, R., Oliphant, T.E., Haberland, M., Reddy, T., Cournapeau, D., Burovski, E., Peterson, P., Weckesser, W., Bright, J., van der Walt, S.J., Brett, M., Wilson, J., Millman, K.J., Mayorov, N., Nelson, A.R.J., Jones, E., Kern, R., Larson, E., Carey, C.J., Polat, I., Feng, Y., Moore, E.W., VanderPlas, J., Laxalde, D., Perktold, J., Cimrman, R., Henriksen, I., Quintero, E.A., Harris, C.R., Archibald, A.M., Ribeiro, A.H., van Mulbregt, P., Vijaykumar, A., Bardelli, A., Rothberg, A., Hilboll, A., Kloeckner, A., Scopatz, A., Lee, A., Rokem, A., Woods, C.N., Fulton, C., Masson, C., Häggström, C., Fitzgerald, C., Nicholson, D.A., Hagen, D.R., Pasechnik, D.V., Olivetti, E., Martin, E., Wieser, E., Silva, F., Lenders, F., Wilhelm, F., Young, G., Price, G.A., Ingold, G.L., Allen, G.E., Lee, G.R., Audren, H., Probst, I., Dietrich, J.P., Silterra, J., Webber, J.T., Slavič, J., Nothman, J., Buchner, J., Kulick, J., Schönberger, J.L., de Miranda Cardoso, J.V., Reimer, J., Harrington, J., Rodríguez, J.L.C., Nunez-Iglesias, J., Kuczynski, J., Tritz, K., Thoma, M., Newville, M., Kümmerer, M., Bolingbroke, M., Tartre, M., Pak, M., Smith, N.J., Nowaczyk, N., Shebanov, N., Pavlyk, O., Brodtkorb, P.A., Lee, P., McGibbon, R.T., Feldbauer, R., Lewis, S., Tygier, S., Sievert, S., Vigna, S., Peterson, S., More, S., Pudlik, T., Oshima, T., Pingel, T.J., Robitaille, T.P., Spura, T., Jones, T.R., Cera, T., Leslie, T., Zito, T., Krauss, T., Upadhyay, U., Halchenko, Y.O., Vázquez-Baeza, Y. (2020). SciPy 1.0: fundamental algorithms for scientific computing in Python. *Nature Methods*, 17(3): 261–272. <https://doi.org/10.1038/s41592-019-0686-2>
32. Paszke, A., Gross, S., Chintala, S., Chanan, G., Yang, E., Lin, Z., Desmaison, A., Antiga, L., Lerer, A. (2017). Automatic differentiation in PyTorch. In *Proceedings of the 31st Conference on Neural Information Processing Systems*.
33. Kingma, D.P., Ba, J.L. (2014). Adam: A Method for Stochastic Optimization. In *3rd International Conference on Learning Representations (ICLR 2015 – Conf. Track Proc.)*. <https://doi.org/10.48550/arXiv.1412.6980>
34. Zhang, T., Pauly, J.M., Levesque, I.R. (2015). Accelerating parameter mapping with a locally low rank constraint. *Magnetic Resonance in Medicine*, 73(2): 655–661. <https://doi.org/10.1002/mrm.25161>
35. Binter, C., Knobloch, V., Manka, R., Sigfridsson, A., Kozerke, S. (2013). Bayesian multipoint velocity encoding for concurrent flow and turbulence mapping. *Magnetic Resonance in Medicine*, 69(5): 1337–1345. <https://doi.org/10.1002/mrm.24370>
36. Yushkevich, P.A., Piven, J., Hazlett, H.C., Smith, R.G., Ho, S., Gee, J.C., Gerig, G. (2006). User-guided 3D active contour segmentation of anatomical structures: significantly improved efficiency and reliability. *NeuroImage*, 31(3): 1116–1128. <https://doi.org/10.1016/j.neuroimage.2006.01.015>
37. Ronneberger, O., Fischer, P., Brox, T. (2015). U-Net: Convolutional Networks for Biomedical Image Segmentation. arXiv preprint. <https://doi.org/10.48550/arXiv.1505.04597>
38. Isensee, F., Jaeger, P.F., Kohl, S.A.A., Petersen, J., Maier-Hein, K.H. (2021). nnU-Net: a self-configuring method for deep learning-based biomedical image segmentation. *Nature Methods*, 18(2): 203–211. <https://doi.org/10.1038/s41592-020-01008-z>
39. Cesario, M., Littlewood, S.J., Nadel, J., Fletcher, T.J., Fotaki, A., Castillo-Passi, C., Hajhosseiny, R., Pouliopoulos, J., Jabbour, A., Olivero, R., Rodríguez-Palomares, J., Kooi, M.E., Prieto, C., Botnar, R.M.: Automated segmentation of thoracic aortic lumen and vessel wall on three-dimensional bright- and black-blood magnetic resonance imaging

using nnU-Net. *J. Cardiovasc. Magn. Reson.* 27, 101923 (2025).
<https://doi.org/10.1016/J.JOCMR.2025.101923>

- 40. Herment, A., Kachenoura, N., Lefort, M., Bensalah, M., Dogui, A., Frouin, F., Mousseaux, E., De Cesare, A. (2010). Automated segmentation of the aorta from phase contrast MR images: Validation against expert tracing in healthy volunteers and in patients with a dilated aorta. *Journal of Magnetic Resonance Imaging*, 31(4): 881–888.
<https://doi.org/10.1002/jmri.22124>
- 41. Bratt, A., Kim, J., Pollie, M. *et al.* Machine learning derived segmentation of phase velocity encoded cardiovascular magnetic resonance for fully automated aortic flow quantification. *J Cardiovasc Magn Reson* 21, 1 (2019). <https://doi.org/10.1186/s12968-018-0509-0>
- 42. Verstraeten, S., Hoeijmakers, M., Tonino, P., Brüning, J., Capelli, C., van de Vosse, F., Huberts, W. (2024). Generation of synthetic aortic valve stenosis geometries for in silico trials. *International Journal for Numerical Methods in Biomedical Engineering*.
<https://doi.org/10.1002/cnm.3778>
- 43. Scuoppo, R., Castelbuono, S., Cannata, S., Gentile, G., Agnese, V., Bellavia, D., Gandolfo, C., Pasta, S. (2024). Generation of a virtual cohort of TAVI patients for in silico trials: a statistical shape and machine learning analysis. *Medical & Biological Engineering & Computing*, 63: 467–482. <https://doi.org/10.1007/s11517-024-03215-8>
- 44. Ostendorf, K., Bäumler, K., Mastrodicasa, D., Fleischmann, D., Preim, B., Mistelbauer, G. (2024). Synthetic surface mesh generation of aortic dissections using statistical shape modeling. *Computer Graphics*, 124: 104070. <https://doi.org/10.1016/j.cag.2024.104070>